Weathering history and landscape evolution of Western Ghats (India) from 40 Ar/ 39 Ar dating of supergene K-Mn oxides

A. Jean, Anicet Beauvais, D. Chardon, N. Arnaud, M. Jayananda, P E Mathe

Weathering history and landscape evolution of Western Ghats (India) from $^{40}Ar/^{39}Ar$ dating of supergene K-Mn oxides

A. Jean[1], A. Beauvais[1*], D. Chardon[2,3], N. Arnaud[4], M. Jayananda[5] & P.E. Mathe[1]

[1] Aix-Marseille Univ, CNRS, IRD, INRA, Coll France, CEREGE, Aix-en-Provence, France

[2] IRD and Département des Sciences de la Terre, Université Joseph Ki-Zerbo, Ouagadougou, Burkina Faso

[3] GET, Université de Toulouse, CNRS, IRD, UPS, CNES, F-31400 Toulouse, France

[4] Université de Montpellier 2, Géosciences Montpellier, UMR CNRS 5243, 34095 Montpellier, France

[5] Centre for Earth, Ocean and Atmospheric Sciences, University of Hyderabad, P.O. Central Gachibowli, Hyderabad 500 046, India

* Correspondence: (beauvais@cerege.fr)

Running title: Western Ghats landscape evolution

Accepted to Journal of the Geological Society
November 05, 2019

DOI: 0.1144/jgs2019-048

Abstract

Laterites preserved on both sides of the Western Ghats Escarpment of Peninsular India have formed by long-term lateritic weathering essentially after India-Seychelles continental break up following Deccan Traps emplacement (c. 63 Ma ago). Supergene manganese ores of the Western Ghats were formed on Late Archean manganese protores. Among Mn oxides composing the ores, cryptomelane (K-rich Mn oxide) was characterized and dated by $^{40}Ar/^{39}Ar$ geochronology. Measured ages complement those previously obtained in other South-Indian manganese ores from the hinterland plateau (Bonnet et al., 2016) and further document three major weathering periods, c. 53-44 Ma, c. 39-22 Ma, and c. 14-10 Ma, the later being documented for the first time in India. These periods coincide with global paleoclimatic proxies and date the lateritic weathering of three successive paleolandscapes of the Western Ghats that evolved under slow denudation (c. 8 m/myr) over the last 44 Myr and were mostly incised during the Neogene (< 22 Ma). That indicates the Western Ghats are a relict of a South Indian plateau preserved at the headwaters of very long east-flowing river systems and above the Western Ghats escarpment. Topography and denudation history of this landscape do not require Neogene tilt of the Peninsula as recently proposed.

Keywords: $^{40}Ar/^{39}Ar$ geochronology – Manganese oxides – Lateritic weathering – Cenozoic – Denudation – Indian Western Ghats

Supplementary material: [Full details of field and samples description, methodology, and analytical data including electron probe microanalyses of cryptomelane, and isotopic analyses and degassing spectra of irradiated cryptomelane grains] is available at

Lateritic regoliths of the continental inter-tropical belt have formed by supergene chemical weathering of rocks and landscape evolution under evolving tropical climates. Over long-time scale, weathering profiles accumulate clays (mainly kaolinite), and metal oxides (Al, Fe, or Mn oxy-hydroxides), which are mostly concentrated in lateritic duricrusts capping the profiles (Bárdossy and Aleva, 1990; Nahon, 1986; Thomas, 1994; Tardy, 1997). Lateritic weathering profiles (up to c.100 m thickness) are currently exposed on relict paleolandsurfaces over large cratonic areas of Africa, South America, Australia and India. Much work was done for dating weathering profiles on most continents of the tropical belt, using $^{40}Ar/^{39}Ar$ dating of K-rich Mn oxides (e.g., Vasconcelos, 1999; Vasconcelos et Conroy, 2003; Beauvais *et al.*, 2008; Bonnet *et al.*, 2016; Deng *et al.*, 2016; Li *et al.*, 2007; Riffel *et al.*, 2015), or (U-Th)/He dating of iron oxy-hydroxides (e.g., Shuster et al., 2005; Vasconcelos et al., 2013; Monteiro *et al.*, 2018; Allard *et al.*, 2018). For instance, ages of cryptomelane formed *in situ* in lateritic regolith of West Africa and Brazil allowed calibrating continental denudation over geological time scales (Beauvais and Chardon, 2013; Vasconcelos and Carmo, 2018). But a reliable geochronological geomorphology is still often lacking to better calibrate the long-term erosion history of many areas of the tropical World that would allow linking lateritic weathering episodes, continental denudation and the evolving paleolandscapes, particularly on passive continental margins and their cratonic hinterlands (e.g., Bonnet et al., 2016).

In Peninsular India, relicts of several generations of stepped lateritic paleolandscapes (termed paleosurfaces) were distinguished (e.g., Widdowson, 1997; Gunnell, 1998), but only recently characterized and dated by $^{40}Ar/^{39}Ar$ radiometry (Bonnet et al, 2014; 2016; Beauvais *et al.*, 2016). Paleolandscape remnants preserved on either side of Western Ghats Escarpment (WGE) separating the coastal lowland plain from a continental-scale high plateau (i.e. the

Karnataka plateau; **Fig. 1b)**, are most numerous upon the Western Ghats proper, i.e., the belt of high topography (800 m - 1500 m) running along the escarpment. These remnant landscapes are key paleotopographic markers of the denudation history of the Peninsula. Three major weathering periods, c. 53-45 Ma, c. 37-26 Ma and c. 26-19 Ma, and two discrete pulses, c. 9 and 2.5 Ma, were previously defined from $^{40}Ar/^{39}Ar$ ages series of cryptomelane, which formed *in situ* in the lateritic profiles and supergene Mn-ore deposits on the highland plateau and coastal lowland plain (Bonnet *et al.*, 2016). These ages combined with regional geomorphological observations imply very slow denudation, c. 5-6 m/myr in the lowland and a maximum of c. 15 m/myr in the highland over the last 50 Myr (Beauvais *et al.*, 2016).

The present study focuses on $^{40}Ar/^{39}Ar$ dating of the cryptomelane-rich Mn ore deposits of North Kanara region in the Western Ghats, which have been loosely dated so far by Neogene palynostratigraphic record in their sedimentary overburden (Krishna Rao *et al.*, 1989a). New data further document the major Cenozoic weathering periods previously identified upon the Karnataka plateau and in the coastal lowland (Bonnet *et al.*, 2016) and reveal for the first time a well-characterized Mid-Miocene (14-10 Ma) weathering period. All the ages obtained here establish the first geochronology of lateritic weathering in the North Kanara region and further document the evolution of Western Ghats landscapes that was previously outlined (e.g., Sethumadhav *et al*., 2010). The geomorphological structuration of the Western Ghats into three major lateritic paleolandscapes and the new ages obtained imply a slow denudation regime varying between c. 4.5 and c. 12.5 m/myr over the last 44 Myr, and limited landscape dissection mostly in the Neogene. These results also document the persistence of a lateritic paleolandscape above the West-facing escarpment as a relict of an Eocene plateau in South India comparable to that of current Southern Africa.

Geological and geomorphological setting of the Western Ghats

Lithologies of North Kanara region consist of Archean gneisses/granites and Late Archean (c. 2.6 Ga) supracrustals comprising greywackes, banded iron formations and quartzite with strips of cherts, phyllites, and shales, as well as some stromatolitic dolomites and limestones (Fig. 2a; Sawkar, 1980; Sethumadhav *et al.*, 2010). Greenschist facies metamorphism and moderate deformation affect the supracrustal sequence (Shivaprakash, 1983; Roy, 1981). Supracrustals of North Kanara constitute the northward extension of the Shimoga greenstone belt, and host many Mn supergene ore deposits (Sethumadhav *et al.*, 2010) as other belts of the Dharwar craton (e.g., Sandur and Chitradurga; **Figs. 1 and 2**) (e.g., Mohopatra et al., 1996; Manikyamba et Naqvi, 1997). Most of the North Kanara ore deposits developed upon phyllites/argilites and cherts forming three hilly structural strips trending NNW-SSE (**Fig. 2a**; Sawkar, 1980).

The Kali River drains the region, sourcing near Diggi east of the escarpment; it first flows eastward then south before turning and incising the escarpment westward (Fig. 2b). Relicts of three lateritic paleolandscapes have been distinguished and mapped on the basis of their regolith, morphology and topography (**Figs. 2b-c and 3**). The first and older one, noted S1, is mostly flat and carries Al-Fe rich laterites, mostly bauxitic, between altitudes of c. 770 m and c. 1000 m (**Figs. 2b-c and 3)**. This S1 paleolandscape is equivalent to the S2 paleosurface described by Gunnell (1998). The second lateritic paleolandscape, noted S2, bears thick weathering profiles rich in kaolinite and iron oxy-hydroxides, which are often duricrusted by an Al-Fe rich duricrust (Bonnet *et al.*, 2016) between altitudes of c. 650 m and c. 930 m (**Figs. 2b-c and 3**). The lateritic weathering profile related to the S2 paleolandscape has been previously interpreted as resulting from the late geochemical epigenetic evolution of bauxites (Krishna Rao *et al.*, 1989b; see also Boulangé, 1986). The two paleolandscapes (S1-S2) form

129 a composite landscape, the S2 relicts being preserved mostly as gentle slopes under scarp-
130 bounded S1 remnants that have undergone limited incision (a few tens of meters) but clear
131 relief inversion before final installation of S2. The composite S1-S2 landscape can reach c.
132 100 m of relief (**Figs. 2c and 3**). This paleolandscape is best preserved near the escarpment
133 (Fig. 2b) and represents the westernmost relict of a more extended low relief and gently
134 sloping S1-S2 paleolandscape on the Karnataka plateau, whose remnants have been also
135 observed on the Chitradurga and Sandur greenstone belts at 900-1100 m elevation (**Fig. 1**; see
136 Bonnet et al., 2016; Beauvais et al., 2016). The third paleolandscape, noted S3, consists of
137 coalescent pediments between c. 750 and 500 m elevation (**Figs. 2c and 3**). The pediments
138 are covered by clay-rich ferruginous soils (Gunnell and Bourgeon, 1997), which can be
139 locally duricrusted. S3 surface once formed a pediplain resulting from the dissection of the
140 composite S1/S2 landscape. The pediplain fossilizes the foot of steep, regolith-free slopes,
141 150 to 250 m in amplitude, which formed by incision of the S1-S2 relict landscape (**Figs. 2c**
142 **and 3**; Bonnet *et al.*, 2016; see also Chardon et al., 2018 and references therein). The S3
143 pediplain therefore integrates relicts of the S1-S2 landscape. The pediplain is incised by about
144 50 to 100 m (locally 300 m by the Kali River valley**, Figs 2b-c and 3**). The regolith
145 underlying the S3 pediment surfaces hosts most of the Mn ore deposits at altitudes ranging
146 from 520 to 650 m (**Fig. 2b and Tab. 1**). The S1-S3 landscape sequence in the Western Ghats
147 is similar to that previously described on the Karnataka plateau (Bonnet et al., 2016).
148
149 **Materials and methods**
150 ***Sampling, characterization and collection of cryptomelane***
151 Eleven samples of Mn-rich duricrusted ore were collected for their richness in
152 cryptomelane on sections and benches of five-abandoned open mine workings of supergene

153 Mn ore deposits et Diggi, Terali, Nagari, Illva and Pradhani (**Figs. 2 and 4a**). Most of
154 collected manganese ores show massive, botryoidally colloform-mineralized structures, or
155 infiltration ore in lateritic iron duricrust rich in cryptomelane and other Mn oxides, as well as
156 secondary goethite (**Figs. 4b-e**). Some samples also show the primary lithological banding of
157 parent rocks and protores.

158 The different operations for identifying, characterizing and sampling cryptomelane grains
159 are summarized in the Figure 3 (see also Bonnet *et al*., 2016). Cryptomelane and other Mn
160 oxides were first identified on fully polished thin sections (200-300 μm-thickness), which
161 were observed under reflected light microscopy and analysed by X-ray micro-fluorescence, μ-
162 XR, (**Figs. 4d-e**). The μ-XRF analysis allowed mapping Mn, K and Fe concentrations on the
163 polished thin sections to identify the area the richest in cryptomelane. Cryptomelane was also
164 analysed by Electron Probe Micro-Analysis (EPMA) in polished thin sections.

165 Additional small grains were extracted from the remaining Mn ore duricrust specimens
166 for observation under a scanning electron microscope and characterization by X-ray
167 diffraction (**Figs. 4f-g**). Cryptomelane grains of 0.5 to 2 mm in size were picked on thick
168 counterparts (500 μm-thickness) of each thin section where K and Mn are both present (**Fig.**
169 **4e**). Fifty-one grains were selected and divided into two batches, one reduced to powder (c. 64
170 μm size fraction) and analysed by XRD (**Fig. 4f**), and the other one kept for dating.

171

172 ***Cryptomelane grain irradiation and $^{40}Ar / ^{39}Ar$ dating***

173 Cleaned and purified cryptomelane grains were conditioned in aluminium foil packets,
174 and placed into an irradiation vessel including also the monitor VN-FCT-98 of Fish Canyon
175 Tuff volcanic (U.S.A.) dated at 28.172 ± 0.028 Ma (Rivera *et al.*, 2011) every ten grains.
176 Isotopic analyses and dating were performed using the step-heating method of irradiated

grains with a CO2 laser emitting in the infrared. Measured isotopic ratios were corrected for irradiation interferences and air contamination using the up-to-date mean $^{40}Ar/^{36}Ar_{atm}$ value of 298.56 ± 0.31 (Lee *et al.*, 2006; Renne *et al.*, 2011).

Plateau ages are generally derived using several apparent ages integrated over continuous degassing steps overlapping at 2σ error level and integrating at least 70% ^{39}Ar released (Fleck, 1977; Maluski, 1985; McDougall and Harrison, 1988). A plateau age is still valid when it integrates 50 % to 70 % of ^{39}Ar released over at least three continuous degassing steps whose individual ages overlap in the 2σ error (e.g., Vasconcelos, 1999; Li and Vasconcelos, 2002; Vasconcelos and Conroy, 2003; Colin *et al.*, 2005; Li *et al.*, 2007; Feng and Vasconcelos, 2007; Vasconcelos *et al.*, 2013; Riffel *et al.*, 2015; Bonnet *et al.*, 2014; Deng *et al.*, 2016). When more than two degassing steps integrate only 40 to 50% of ^{39}Ar released in the 2σ level, a "pseudo-plateau" age was preferred (Vasconcelos *et al.*, 2013; Riffel *et al.*, 2015). When at least three consecutive reasonably flat steps do not strictly overlap in the 2σ level, a "forced" plateau was required to calculate an age weighted by error and the ^{39}Ar released for each degassing step (Vasoncelos *et al.*, 2013; Riffel *et al.*, 2015).

Picked cryptomelane are generally pure, but sometimes, hypogene contaminations (muscovite), mixed cryptomelane generations, or cryptomelane mixed with authigenic phases (e.g., todorokite ($(Na,Ca,K)_2(Mn^{4+},Mn^{3+})_6O_{12}$•3-4.5($H_2O$)) result in very perturbed degassing spectra including analysis biases and dating errors. For such cases, although pseudo-plateau and forced plateau ages can be estimated, the $^{36}Ar/^{40}Ar$ vs. $^{39}Ar/^{40}Ar$ correlation diagrams may be required to derive age from best-fitted isochron with a mean square weighted deviation (MSWD) as close as possible to 1 (ideally less than 2.5; see Roddick *et al.*, 1980) and a $^{40}Ar/^{36}Ar$ intercept as close as possible to the air value of 298.56 in the 2σ error level.

Results and interpretations

Characterization and stoichiometric composition of cryptomelane

All samples contain mostly cryptomelane (**Fig. 4d-f**), but iron oxy-hydroxides such as goethite and sometimes hematite were also identified**,** with other manganese oxy-hydroxides, i.e., lithiophorite ((Al, Li) $Mn^{4+}O_2(OH)_2$), nsutite (γ-MnO_2) (see **Figs. 4d-e**), and even pyrolusite (β-MnO_2). Similar Mn oxides have been previously described in same Mn ore deposits of Western Ghats (Sethumadhav *et al*., 2010). The relative richness in iron oxide such as goethite is linked to banded iron formations associated with phyllites/argillites. Quartz and muscovite were also determined as minor components.

The stoichiometric compositions of cryptomelane were calculated from EPMA and plotted in a ternary diagram (**Fig. 5**). Some microanalyses from Nagari Mn deposit samples have relatively high aluminium content owing to possible intergrowth with lithiophorite, or mixture with a primary mineral like muscovite inherited from parent phyllites and argilites (Bonnet *et al.*, 2016). Microanalyses from Pradhani samples show high Fe content up to 20 wt.%. Cryptomelane from Terali deposit can be Al-rich (**Fig. 5**) owing to relict muscovite. Cryptomelane from Diggi, Illva and some from Pradhani have less aluminous impurities (Al never exceeding 2.73 wt.%, **Fig. 5**).

Weathering geochronology of the Western Ghats

Fifty-one cryptomelane grains collected in samples from five Mn ore deposits were analysed and dated, and thirty-eight have significant geological ages (**Tab. 1**). Synthetic results presented in the Table 1 allow distinguishing three family or groups of ages, Mid-Miocene (**Fig. 6**), Early Miocene – Late Eocene (**Fig. 7**), and Mid-Eocene (**Fig. 8**).

225 *Overview of ^{39}Ar release spectra*

226 Fifteen grains have homogenous degassing spectra allowing calculation of plateau ages
227 integrating 70 to 90 % of ^{39}Ar released and thirteen with 50 to 70 % of ^{39}Ar released (**Tab. 1**,
228 **Figs. 6 and 8**). Many irradiated grains picked in the same sample have reproducible
229 homogeneous degassing spectra. Seven spectra do not strictly respect the overlap upon the 2σ
230 error that requires calculation of acceptable age from forced plateaus and/or best-fitted
231 isochrons in correlation diagrams (**Figs. 7 and 8 and Tab. 1**).

232 Three types of perturbed degassing spectra have been identified. Hump-shape degassing
233 spectra, tagged HS (see **Figs. 7 and 8**) typify a mixture of at least two cryptomelane
234 generations that only allow estimating the minimum age of the oldest phase and the maximum
235 age of the youngest phase (Beauvais *et al.*, 2008). Saddle shape degassing spectra, tagged SS
236 (**Fig. 7**) result from mixture of several supergene phases, or contamination by a hypogene
237 mineral (Hautmann et Lippolt, 2000; Ruffet *et al.*, 1996; Vasconcelos *et al.*, 1995). Staircase-
238 degassing spectra, tagged SD, suggest possibly a system opening, or a mixing of different
239 cryptomelane generations with a disturbance at high energy, owing generally to a
240 contamination by a hypogene phase (**Fig. 7**).

241

242 *Mid-Miocene cryptomelane ages*

243 Most of the Mid-Miocene ages have been calculated for cryptomelane of samples
244 collected in Diggi and Illva Mn ore deposits (**Figs. 6a-b**). Three grains, DIG-1A-T4 to T6,
245 picked in the same thick section, have very similar degassing spectra allowing to derive
246 reproducible plateau ages between c.11 and c.12 Ma integrating more than 70 % of ^{39}Ar (**Fig.**
247 **6a**). Two other grains DIG-1B-T2 to T3 have a same age of c.13 Ma. The first one (DIG-1B-
248 T2) is a "pure" cryptomelane grain, with a regular ^{39}Ar-releasing spectrum allowing to

calculate a meaningful plateau age, based on 85 % ^{39}Ar released. The second one (DIG-1B-T3), picked in the same thick section, has a plateau like degassing spectrum with 79 % ^{39}Ar released confirming the reproducibility of plateau age calculation for the two grains (**Fig. 6a**). Grain DIG-1B-T4 is also a "pure" cryptomelane characterized by a regular degassing spectrum with 74 % ^{39}Ar released, providing a robust plateau age of c.12 Ma.

One grain (ILV-1B-T4) has a homogeneous degassing spectrum providing plateau ages of c. 13 Ma integrating more than 90 % ^{39}Ar released (**Fig. 6b**). Two others grains picked in botryoïdal crystallizations from a same thick section (ILV-2C-T3 and -T4) also have reproducible homogenous degassing spectra with robust plateau ages of c.12 to c.13 Ma accounting for more than 80 % of ^{39}Ar released. Grain ILV-3C-T4 picked in allochthonous Mn ore sample has degassing spectra allowing calculation of a plateau age of c. 14 Ma integrating more than 60 % ^{39}Ar released (**Fig. 6b**). Two other grains picked in a same thick plate have reproducible degassing spectra providing plateau age of c. 12 Ma (ILV-6A-T2) and c. 10 Ma (ILV-6A-T3) both integrating c. 80 % of ^{39}Ar released.

Late Eocene to Early Miocene Cryptomelane ages

This group (**Fig. 7**) comprises ages obtained for cryptomelane of samples from deposits of Terali and Pradhani. Two cryptomelane rich grains (TER-1A-T1, TER-1B-T3) have degassing spectrum with a slight hump-shape (**Fig. 7a**) suggesting mixture of two cryptomelane generations. Such spectra allow defining only forced plateau ages c. 29 and c. 27.5 Ma, respectively, both accounting for at least 60% ^{39}Ar released.

One grain (PRA-1B-T1) is characterized by a staircase-degassing spectrum (**Fig. 7b**), which at best allows estimating poorly robust pseudo or forced plateau ages c. 25 Ma integrating 61 % of ^{39}Ar released. Three cryptomelane grains (PRA-2A-T1, -T3 and -T5) have similar slight

staircase degassing spectra allowing to derive plateau ages of c. 24.5 Ma, c. 23.7 and c. 21.6, integrating 58 to 78-79 % of ^{39}Ar released, respectively (**Fig. 7b**). The degassing spectra of the other four grains (PRA-2B-T1, -T4; PRA-3B-T1, and -T2) provide plateau and/or forced plateau ages varying from c. 23 Ma to c. 37.5 Ma (**Fig. 7 and Tab. 1**). Two grains (PRA-3B-T1 –T2) have reproducible "saddle shape" spectra (**Fig. 7b**) suggesting opened systems and/or supergene phase's mixture with a hypogene phase at high energies. Nonetheless, plateau and forced plateau accounting for more than 50 % of ^{39}Ar released, allow deriving ages c. 32.8 and c. 37.5 Ma *(***Tab. 1**), which may be the less poorly estimated maximum ages.

Mid-Eocene cryptomelane ages

Most of Mid-Eocene cryptomelane grains (**Fig. 8**) were picked in samples from the deposits of Nagari and Pradhani (**Tab. 1**). Two grains picked in the same thick section (NAG-3B-T1 and T2) have a more or less homogenous degassing, allowing calculation of plateau ages at c. 45 and c. 44 Ma, respectively (**Fig. 8a**). The ^{39}Ar release spectrum of NAG-3B-T2 shows a slight hump shape with three steps accounting for 78 % of ^{39}Ar released and overlapping in 2σ error, which provides a reliable plateau age. The last grain NAG-3B-T3 has a perturbed ^{39}Ar release spectrum resulting from mixing of cryptomelane generations that only allows consideration of a forced plateau age c. 45 Ma accounting for more than 50 % of ^{39}Ar release (**Fig. 8a**). Grain PRA-1B-T3 has a pronounced hump-shape degassing spectrum typifying phases mixing that provide only a forced-plateau age of c. 45 Ma accounting for 50 % of ^{39}Ar released **(Fig. 8b).**

Summary and interpretation of the ^{40}Ar/^{39}Ar ages

The three groups of ages (Table 1), c. 45-44 Ma, c. 37.5-22 Ma, and c. 14-10 Ma, complement ages obtained previously in other manganese ore deposits from the Karnataka

plateau (Sandur) and Western Ghats (Shimoga) south of the present study area that further document the weathering periods previously established by Bonnet *et al.* (2016): Eocene and Oligocene-Early Miocene, with a new period in Mid-Miocene. Altogether, the ages define three main weathering periods, c. 53 to c. 44 Ma (W1), c. 39 to c. 22 Ma (W2), and c. 14 to c. 10 Ma (W3). Those periods mostly coincide with warm and humid climatic global trends (**Fig. 9**), which were potentially conducive to intense lateritic weathering in the Peninsula as well on most continents of the tropical belt (Retallack, 2010). Under such conditions, and especially during the two first periods W1 and W2, relatively fast deepening of weathering fronts (up to 10 m/myr; Boulangé et al., 1997; see also Tardy and Roquin, 1992) allowed early segregation of aluminium, iron and manganese, controlled by their relative mobility (Eh- and pH-dependent) in weathering profiles and landscapes (Melfi and Pedro, 1974; Hem, 1981; Beauvais *et al*., 1987). Early weathering of parental minerals such as illite or muscovite into kaolinite or gibbsite released K^+ ions required to form cryptomelane (Parc et al., 1989). Like in West Africa (Beauvais et al., 2008) or upon the Karnataka plateau (Bonnet et al., 2014, 2016), Al-Fe-Mn geochemical differentiations have resulted in early formation of manganese ore deposits including K-rich Mn oxides (cryptomelane) at depth in the profiles of the S1 bauxitic paleolandscape **(Fig. 10a)**. Such a surface geochemical dynamics typifies the weathering regime of cratonic tropical regions, where slow base level lowering warranties coeval landscape incision/dissection and long lasting deepening of weathering fronts. A slight change in climatically driven surface erosional processes after c. 44 Ma (**Fig. 9**) allowed for the abandonment of a duricrust-capped paleosurface S1 and installation of the S2 surface without stripping the entire thickness of the S1 bauxitic weathering profile **(Fig. 10b)**. A comparable scenario applies for the abandonment of S2 and installation of S3, even though S3 has allochtonous clasts of older weathered material dispersed on its surface. Such a

punctuated erosion-weathering regime therefore allowed for the preservation of early-formed weathering materials including manganese ores rich in cryptomelane in the S1 profiles, as well as in those of S2 and S3 (**Fig. 10b-c**). Therefore, the weathering profiles of the youngest S3 surface were able to host and keep record of "the roots" of manganese-rich profiles formed during the S1 and S2 stages (**Fig. 10c**). The minimum age of weathering periods marks the stabilization of weathering fronts at each stage responding to the lowering of base levels resulting in landscape dissections and the abandonment of S1 at c. 44 Ma, S2 at c. 22 Ma, and S3 at c. 10 Ma **(Figs. 10a-c)**. The time intervals between the age groups, i.e., 44-39 Ma, 22-14 Ma, and 10-0 Ma (**Fig. 9**) document periods of subdued weathering under seasonally drier climatic conditions with correlative landscape dissection and evolution into three stepped lateritic paleolandscapes, S1 to S3 (**Figs. 2c and 3;** see also Beauvais and Chardon, 2013). Therefore, the Western Ghats have seen their early low-relief S1 landscape differentiated during three major denudation periods bounded by terminal ages of W1, W2, W3 and the present-day, i.e., 44-22 Ma, 22-10 Ma, and 10-0 Ma.

Weathering and morphoclimatic history of the Western Ghats

Early to Mid Eocene weathering period, W1 (53 - 44 Ma)

The Eocene period documented here by four ages around 44-45 Ma attests to the minimum age boundary of this first weathering period (**Fig. 9**), which begun at least c. 53 Ma ago as documented further east at Sandur (Bonnet *et al.*, 2016). The Eocene is known as a period of bauxitization worldwide, particularly from cratonic domains of the inter-tropical belt (Prasad, 1983; Valeton, 1999; Retallack, 2010). This first weathering period of at least 9 Myr coincided with the global Early Eocene climatic optimum (c. 50 Ma; **Fig. 9**), and occurred in Peninsular India less than c. 5 Myr after the Paleocene-Eocene Thermal

346 Maximum and the onset of Himalayan collision c. 55-57 Ma ago (Hu et al., 2016; Najman et
347 al., 2010). During this period, India slowed its northward drift across the mostly equatorial
348 inter-tropical zone (Tardy and Roquin, 1998; Kent and Muttoni, 2008; see Bonnet et al.,
349 2016) and intense lateritic weathering, with segregation of aluminium from iron and
350 manganese in thick, mostly bauxitic profiles, affected most of lithologies including the
351 Deccan Traps (Bardossy and Aleva, 1990; Krishna Rao *et al.*, 1989b; Valeton, 1999).
352 Remnants of such bauxitic paleolandscapes (S1) are distributed in the Western Ghats and
353 locally preserved on the Karnataka plateau (Bonnet *et al.*, 2016). After 44 Ma, the S1 bauxitic
354 paleolandscape was reworked (see Krisna Rao et al., 1989b) allowing the establishment of the
355 S2 paleolandscape (**Figs. 2c, 3 and 10b**).
356
357 ***Late Eocene - Early Miocene weathering period, W2 (39 - 22 Ma)***
358 This long weathering period (c. 17 Myr) in the Western Ghats is documented by fifteen
359 ages complementing those previously obtained in Sandur on the Karnataka plateau and in
360 Shimoga (Western Ghats south of the Kanara district studied here) between 39 Ma and 23 Ma
361 (Bonnet *et al.*, 2016). The oldest ages obtained in the Western Ghats (c. 37.5 Ma in the
362 present study and c. 39 Ma in Shimoga) document that lateritic weathering might have been
363 enhanced in South India by monsoon-like climatic regimes recently reported by authors
364 (Dupont-Nivet *et al.*, 2008; Licht *et al.*, 2014). This weathering period occurred a few million
365 years after the onset of global Mid-Eocene Climatic Optimum (c. 42 Ma; **Fig. 9**).
366 Late Eocene ages (c. 39 Ma) were obtained on cryptomelane in Shimoga Mn ore deposit
367 upon the S2 paleosurface (Bonnet et al., 2016; **Fig. 9**) and on kaolinite from a relict truncated
368 weathering profile from the southernmost Western Ghats in the upslope part of Kavery River
369 drainage (see Mathian *et al.*, 2019). This means that both minerals formed simultaneously at

370 the onset of lateritization and morphogenesis of S2 paleolandscape (**Fig. 10b**). Old concordant
371 ages obtained on the Karnataka plateau as well as in the Western Ghats belt are attributed to
372 the S2 paleolandscape that evolved slowly during a long-lasting period (c. 17 Myr) of intense
373 lateritic weathering, potentially under seasonally tropical humid climate.
374 The numerous ages between c. 30 and 23 Ma (**Tab. 2 and Fig. 9**) confirm those
375 previously obtained in Sandur and Shimoga (**Fig. 1a;** Bonnet *et al*., 2016) and document
376 enhanced weathering of S2 paleolandscape at the Oligocene-Miocene transition. These ages
377 bracket the global late Oligocene warming (LOW) at c. 26 Ma (**Fig. 9**), during which modern-
378 like monsoon regimes might have installed on the Peninsula (Chatterjee *et al*., 2013), with a
379 western/eastern rainfall contrast comparable to the modern one. Therefore, more humidity
380 supported intense lateritic weathering upon the Western Ghats and below the escarpment,
381 while further aridity and landscape dissection prevailed in the interior plateau, e.g., Sandur
382 where weathering was subdued from c. 26 Ma (**Fig. 8**; see also Bonnet *et al*., 2016). The
383 weathering period ended c. 22 Ma ago with the abandonment of paleolandscape S2 (**Fig.**
384 **10b**). Afterwards, landscape dissection prevailed in the Western Ghats and the S3
385 paleolandscape established (**Figs. 2c, 3 and 10c**).
386
387 ***Mid-Miocene weathering period, W3 (14 - 10 Ma)***
388 The mid-Miocene weathering period W3 is relatively short (c. 4 myr) but well
389 documented by eighteen ages in the Western Ghats, and coincided with the global Mid-
390 Miocene Climatic Optimum (**Fig. 9**). The ages also agree with palynostratigraphy in the same
391 Mn deposits (Krishna Rao *et al.*, 1989a), and document renewed lateritic weathering in the
392 Western Ghats once the S3 pediplain landscape was established (**Figs. 2c, 3 and 10c**). After c.
393 10 Ma, landscape dissection that formed the current incised valleys (**Fig. 2c)** would have been

coeval with apparently subdued weathering attested to by the lack of ages (**Fig. 9**). However, late Neogene ages (9 and 2.5 Ma) were previously recorded on cryptomelane in the coastal lowland (Bonnet et al., 2016) or further south (9, 3.5 and 1 Ma) on kaolinite in the Western Ghats (Mathian et al., 2019). Those weathering pulses date landsurface processes responses to Neogene monsoon regimes, which are particularly marked in the Western Ghats and the western lowland due to the orographic effect of the WGE (Bonnet *et al*., 2016).

Landscape evolution of the Western Ghats

The well-preserved S1-S2 composite paleolandscape of Western Ghats has been mostly shaped by c. 18 Myr of cumulated chemical weathering (45 to 44 and 39 to 22 Ma; **Fig. 9**) and moderate denudation between 44 and 39 Ma (**Figs. 2c and 10a-b**). Most of the dissection of that landscape occurred from 22 to 14 Ma during which the S3 pediplain grew at its expenses (**Figs. 2c, 3 and 10c)**. Then, after a short episode of weathering (4 Myr), the S3 paleolandscape was finally dissected over the last 10 Myr. Therefore, after abandonment of S1 paleolandscape 44 Ma ago (**Fig. 10a**), the Western Ghats relief gradually increased up to 350 m by punctuated base level falls (**Fig. 2c**), implying a maximal denudation rate of c. 8 m/myr over the last 44 Myr. In detail, the maximum 350 m of relief production in Western Ghats may be divided into three steps correlated to the abandonment of each paleolandscape, S1 to S3 (**Figs. 2c, 3 and 10**). First, a maximum elevation difference of 100 m between S1 (44 Ma) and S2 (22 Ma) implies a maximum denudation rate of 4.5 m/myr, which is mostly chemical (**Fig. 9**). Then, a maximum of 150 m elevation between S2 and S3 (**Figs. 2c, 3 and 10b-c**) implies 12.5 m/myr of maximum denudation rate between 22 Ma and 10 Ma. Finally, the 100 m of maximum elevation difference between S3 and the current local base level in the upstream area of the Kali River drainage basin (**Figs. 2c and 3**) implies a river incision rate

418 that did not exceed 10 m/myr over the last 10 Myr. Locally, 300 m-deep gorges of the Kali
419 River imply imply an incision rate of 30 m/myr.
420 The estimated denudation rates are similar to millennial-scale erosion rates derived from
421 ^{10}Be cosmogenic radionuclides measurements (CRN) on the southern Karnataka plateau
422 (Gunnell *et al.*, 2007), or slightly lower than ^{10}Be-derived estimate (c. 15 m/myr) in river
423 borne sediments from the same region (Mandal *et al*., 2015). Although time scale (1 myr) and
424 hypotheses of CRN methods complicate comparisons, altogether same order estimates
425 derived from different time scales typify slow, steady state denudation regimes of landscapes
426 mostly controlled by climate rather than by epeirogeny (Beauvais and Chardon, 2013).
427 Over the last 22 Myr, slow denudation (c. 11 m/myr) and dissection have preserved a
428 Paleogene S1-S2 smooth paleolandscape over the Western Ghats (**Figs. 2b-c, 3 and 10b-c**).
429 This antique paleolandscape is the remnant of a South Indian plateau that once occupied most
430 of the peninsula, comparable to the current Southern African Plateau (Partridge and Maud,
431 1987; Burke and Gunnell, 2008). The great extension of the South Indian plateau is attested
432 to, for instance, by the preservation of large areas of smooth bauxitic paleolandscapes at 900-
433 1450 m elevation in the Eastern Ghats (Bardossy and Aleva, 1990; see also Subramanian and
434 Mani, 1979) or by the Sandur relict of the S1-S2 paleolandscape more than 250 km inland the
435 WGE (Bonnet *et al*., 2016). The current E-W asymmetric and eastward sloping topographic
436 profile of the Peninsula (e.g., Gunnell, 1998; Richards et al., 2016) would be due to the
437 regressive erosion of the plateau by the long east-flowing river systems that mostly preserved
438 a plateau relict near their headwaters, right above the Western Ghats escarpment as well as
439 residual patches such as the Eastern Ghats (Jean, 2019). The asymmetrically eroded plateau
440 model proposed here is an alternative to the c. 20 Ma eastward tilt model of the Peninsula
441 proposed by Richards *et al*. (2016) to explain the current eastward slope of Southern India.

Indeed, negligible Neogene denudation rates documented on either side of the WGE (Beauvais *et al*., 2016; Bonnet *et al*., 2016; present work) imply that the escarpment is at least 50 Ma old and challenge the popular model of uplift and/or rejuvenation of the escarpment in the Neogene advocated by most authors (e.g., Radhakrishna, 1993; Widdowson and Gunnell, 1999; Mandal *et al.*, 2017). Furthermore, combined geomorphology and Ar-Ar geochronology of the western coastal lateritic lowland of the Peninsula infers negligible uplift since c. 50 Ma (Beauvais *et al*., 2016; Bonnet *et al*., 2016). Therefore, geomorphological observations and denudation rates quantified by Ar-Ar geochronology preclude the eastward tilt model of Richard *et al*. (2016) that requires 30 to 100 m/myr of uplift - and thus rejuvenation - of the Western margin of the Peninsula since 23 Ma. Our results also imply that the largest volume of sediments produced from the dissection of the South Indian plateau was routed towards the eastern margin of the Peninsula.

Conclusions

The $^{40}Ar/^{39}Ar$ ages of cryptomelane from supergene manganese ores of the Western Ghats document three major weathering periods in South India: Early-Mid-Eocene (W1), Late Eocene-Early Miocene (W2) and Mid-Miocene (W3). These weathering periods coincide with known global and regional climatic proxies and alternated after c. 22 Ma with periods of subdued weathering during which landscape has been structured step by step into three composite lateritic paleolandscapes S1, S2 and S3. The minimum age of each weathering period determines the abandonment of each paleolandscape, i.e., S1 at 44 Ma, S2 at 22 Ma and S3 at 10 Ma, which bound three major periods of landscape denudation and shaping, i.e., 44-22 Ma, 22-10 Ma and 10-0 Ma. Maximum Cenozoic denudation rates in Western Ghats range from 4.5 to 12.5 m/myr, which confirms previous estimates in South India (Beauvais *et*

al., 2016). Our results document very long-term slow denudation of tropical cratonic mountains typified by the Western Ghats. That persistent topography is a relict of a South Indian lateritic plateau of Eocene age.

Acknowledgements – This work is part of AJ PhD thesis, funded by the Indo-French Centre for the Promotion of Advanced Research (IFCPAR) project 5007-1, the CNRS (INSU-2017- programme TelluS-SYSTER) and the IRD (UMR 161 CEREGE). The Karnataka State Forest Department (Wild Life Division) is gratefully acknowledged for guidance and logistic support. The French Ministry for Scientific Research and Education granted AJ a PhD scholarship (ED251, Aix Marseille Université, Obervatoire des Sciences de l'Univers Pytheas). This work also benefited of technical support from D. Borschneck, Cerege (XRD and μ-XRF analyses), B. Boyer (EPMA), and M. Bonno, A. Iemmolo, D. Jourdain, C. Lanvin, P. Monié, P. Münch (Argon radiochronology), from Geosciences Montpellier. We thank Peter Van der Beek for his remarks on a first draft, and suggestions from reviews of Cécile Gautheron and Gregory Retallack. Igor Maria Vila is thanked for editorial handling.

Funding information

IFCPAR (5007-1); INSU-2017- programme TelluS-SYSTER; IRD recurrent funding

References

Allard, T., Gautheron, C., Riffel, S.B., Balan, E., Soares, B.F., Pinna-Jamme, R., Derycke, A., Morin, G., Bueno, G.T. & do Nascimento, N. 2018. Combined dating of goethites and kaolinites from ferruginous duricrusts. Deciphering the Late Neogene erosion history of Central Amazonia. *Chemical Geology*, **479**, 136-150.

Bárdossy, G. & Aleva, G.J.J. 1990. Lateritic Bauxites. *Elsevier Science*. Amsterdam; New

491 York, 624 p.
492 Beauvais, A., Bonnet, N.J., Chardon, D., Arnaud, N. & Jayananda, M. 2016. Very long-term
493 stability of passive margin escarpment constrained by $^{40}Ar/^{39}Ar$ dating of K-Mn oxides.
494 *Geology*, **44**, 299–302.
495 Beauvais, A. & Chardon, D. 2013. Modes, tempo, and spatial variability of Cenozoic cratonic
496 denudation: The West African example. *Geochemistry, Geophysics, Geosystems*, **14**,
497 1590–1608.
498 Beauvais, A., Melfi, A., Nahon, D. & Trescases J-.J. 1987. Pétrologie du gisement latéritique
499 managnésifère d'Azul (Brésil). *Mineralium Deposita*, **22**, 124-134.
500 Beauvais, A., Ruffet, G., Hénocque, O. & Colin, F. 2008. Chemical and physical erosion
501 rhythms of the West African Cenozoic morphogenesis: The ^{39}Ar-^{40}Ar dating of
502 supergene K-Mn oxides. *Journal of Geophysical Research: Earth Surface*, **113,** F04007.
503 Bonnet, N.J., Beauvais, A., Arnaud, N., Chardon, D. & Jayananda, M. 2014. First $^{40}Ar/^{39}Ar$
504 dating of intense Late Palaeogene lateritic weathering in Peninsular India. *Earth and*
505 *Planetary Science Letters*, **386**, 126–137.
506 Bonnet, N.J., Beauvais, A., Arnaud, N., Chardon, D. & Jayananda, M. 2016. Cenozoic
507 lateritic weathering and erosion history of Peninsular India from $^{40}Ar/^{39}Ar$ dating of
508 supergene K–Mn oxides. *Chemical Geology*, **446**, 33–53.
509 Boulangé, B., 1986. Relation between lateritic bauxitization and evolution of landscape.
510 *Travaux du Comité International pour l'Etude des Bauxites, de l'Alumine et de*
511 *l'Aluminium* (ISCOBA), **16–17**, 155-162.
512 Boulangé, B., Ambrosi, J.-P. & Nahon, D. 1997. Laterites and bauxites. In *Soils and*
513 *sediments: Mineralogy and geochemistry*, Paquet, H. &Clauer, N. eds., Springer, Berlin,
514 49-65.

515 Burke, K. & Gunnell, Y. 2008. The African erosion surface: A continental-scale synthesis of
516 geomorphology, tectonics, and environmental change over the past 180 million years.
517 *Geological Society of America, Memoir*, **201**, 80.
518 Chardon, D., Grimaud, J.L., Beauvais, A. & Bamba, O. 2018. West African lateritic
519 pediments: Landform-regolith evolution processes and mineral exploration pitfalls.
520 *Earth-Science Reviews*, **179**, 124-146.
521 Chardon, D., Jayananda, M., Chetty, T.R & Peucat J.J. 2008. Precambrian continental strain
522 and shear zone patterns/ south Indian case. *Journal of Geophysical Research*, 113,
523 B08402.
524 Chatterjee, S., Goswami, A. & Scotese, C.R. 2013. The longest voyage: Tectonic, magmatic,
525 and paleoclimatic evolution of the Indian plate during its northward flight from
526 Gondwana to Asia. *Gondwana Research*, **23**, 238–267.
527 Colin, F., Beauvais, A., Ruffet, G. & Hénocque, O. 2005. First $^{40}Ar/^{39}Ar$ geochronology of
528 lateritic manganiferous pisolites: Implications for the Palaeogene history of a West
529 African landscape. *Earth and Planetary Science Letters*, **238**, 172–188.
530 Deng, X.-D., Li, J.-W. & Vasconcelos, P.M. 2016. $^{40}Ar/^{39}Ar$ dating of supergene Mn-oxides
531 from the Zunyi Mn deposit, Guizhou Plateau, SW China: Implications for chemical
532 weathering and paleoclimatic evolution since the late Miocene. *Chemical Geology*, **445**,
533 185–198.
534 Dupont-Nivet, G., Hoorn, C. & Konert, M. 2008. Tibetan uplift prior to the Eocene-Oligocene
535 climate transition: Evidence from pollen analysis of the Xining Basin. *Geology*, **36**, 987–
536 990.
537 Feng, Y.-X. & Vasconcelos, P. 2007. Chronology of Pleistocene weathering processes,
538 southeast Queensland, Australia. *Earth and Planetary Science Letters*, **263**, 275–287.

539 Fleck, R.J., Sutter, J.F. & Elliot, D.H. 1977. Interpretation of discordant $^{40}Ar/^{39}Ar$ age-spectra
540 of mesozoic tholeiites from antarctica. *Geochimica et Cosmochimica Acta*, **41**, 15–32.
541 Grimaud, J.L., Chardon, D. & Beauvais, A. 2014. Very long-term incision dynamics of big
542 rivers. *Earth and Planetary Science Letters*, **405**, 74-84.
543 Gunnell, Y. 1998. The interaction between geological structure and global tectonics in
544 multistroyed landscape development: a denudation chronology of the South Indian shield.
545 *Basin Research*, **10**, 281–310.
546 Gunnell, Y. & Bourgeon, G. 1997. Soils and climatic geomorphology on the Karnataka
547 plateau, peninsular India. *Catena*, **29**, 239-262.
548 Gunnell, Y., Braucher, R., Bourlès, D. & André, G. 2007. Quantitative and qualitative
549 insights into landform erosion on the South Indian craton using cosmogenic nuclides and
550 apatite fission tracks. *Geological Society of America Bulletin*, **119** (5/6), 576-585.
551 Hautmann, S. & Lippolt, H.J. 2000. $^{40}Ar/^{39}Ar$ dating of central European K-Mn oxides - a
552 chronological framework of supergene alteration processes during the Neogene.
553 *Chemical Geology*, **170**, 37–80.
554 Hem, J.D. 1981. Rates of manganese oxidation in aqueous system. G*eochimica et*
555 *Cosmochimica Acta*, **45**(8), 1369-1374.
556 Hu, X., Garzanti, E., Wang J., Huang, W., An W. & Webb A. The timing of India-Asia
557 collision onset – Facts, theories, controversies. *Earth-Science reviews*, **160**, 264-299.
558 Jean, A. Histoire de la denudation en Inde Péninsulaire: Contraintes des ages $^{40}Ar/^{39}Ar$ des
559 oxydes de manganese supergenes et des reconstructions topographiques des paléo-
560 paysages latéritiques. PhD Thesis, Aix-Marseille University, Marseille, France.
561 Kent, D.V. & Muttoni, G. 2008. Equatorial convergence of India and early Cenozoic climate
562 trends. *Proceedings of the National Academy of Sciences*, **105**, 16065–16070.

563 Krishna Rao, B., Muzamil Ahmed, M. & Janardhana, M.R. 1989a. Age of manganiferous
564 laterite of Uttara Kanada district, Karnataka. *Journal of Geological Society of India*, **34**,
565 413–420.
566 Krishna Rao, B., Satish, P.N. & Sethumadhav, M.S. 1989b. Syngenetic and epigenetic
567 features and genesis of the bauxite-bearing laterite of Boknur-Navge plateau, Belgaum
568 district, Karnataka. *Journal of Geological Society of India*, **34**, 46–60.
569 Lee, J.-Y., Marti, K., Severinghaus, J.P., Kawamura, K., Yoo, H.-S., Lee, J.B. & Kim, J.S.
570 2006. A redetermination of the isotopic abundances of atmospheric Ar. *Geochimica et*
571 *Cosmochimica Acta*, **70**, 4507–4512.
572 Li, J.-W., Vasconcelos, P., Duzgoren-Aydin, N., Yan, D.-R., Zhang, W., Deng, X.-D., Zhao,
573 X.-F., Zeng, Z.-P., Hu, M.-A.. 2007. Neogene weathering and supergene manganese
574 enrichment in subtropical South China: An $^{40}Ar/^{39}Ar$ approach and paleoclimatic
575 significance. *Earth and Planetary Science Letters*, **256**, 389–402.
576 Licht, A., van Cappelle, M., Abels, H. A., Ladant, J.-B., Trabucho-Alexandre, J., France-
577 Lanord, C., Donnadieu, Y., Vandenberghe, J., Rigaudier, T., Lécuyer, C., Terry Jr, D.,
578 Adriens, R., Boura, A., Guo, Z., Soe, A.N., Quade, J., Dupont-Nivet, G., Jaeger, J.-J.
579 2014. Asian monsoons in a late Eocene greenhouse world. *Nature*, **513**, 501–506.
580 McDougall, I. & Harisson, T.M. 1988. Geochronology and Thermochronology by the
581 $^{40}Ar/^{39}Ar$ Method, *Oxford University Press.*, New York, 62 p.
582 Maluski, H. 1985. Méthode argon 39-argon 40. Principe et applications aux minéraux des
583 roches terrestres. *E Roth, B Poty (Eds.)*, Méthodes de Datation par les Phénomènes
584 Nucléaires Naturels, Masson, Paris, 341-372
585 Mandal, S.K., Burg, J.P. and Haghipour, N., 2017. Geomorphic fluvial markers reveal
586 transient landscape evolution in tectonically quiescent southern Peninsular India.

587 *Geological Journal*, **52**(4), 681–702.
588 Mandal, S.K., Lupker, M., Burg, J.P., Valla, P.G., Haghipour, N. & Christl, M. 2015. Saptial
589 variability of ^{10}Be-derived erosion rates across the southern Peninsular Indian
590 escarpment : A key to landscape evolution across passive margins. *Earth and Planetary*
591 *Science Letters*, **425**, 154-167.
592 Manikyamba, C. & Naqvi, S.M. 1997. Mineralogy and geochemistry of Archaean greenstone
593 belt-hosted Mn formations and deposits of the Dharwar Craton: Redox potential of proto-
594 oceans. *Geological Society London Special Publication*, **119**, 91–103.
595 Mathian, M., Aufort, J., Braun, J.J., Riotte, J., Selo, M., Balan, E., Fritsch, E., Bhattacharya,
596 S. & Allard , T. 2019. Unraveling weathering episodes in Tertiary regoliths by kaolinite
597 dating (Western Ghats, India). *Gondwana Research*, **69**, 89-105.
598 Melfi, A.J. & Pedro, G. 1974. Etude sur l'altération expérimentale des silicates de manganèse
599 et la formation exogène des gisements de manganèse..*Bulletin du Groupe Français des*
600 *argiles*, **26**, 91-95.
601 Mohopatra, B.K., Rao, D.S., Nayak, B.D. & Sahoo, R.K. 1996. Mineralogical and chemical
602 charcateristics of ferromanganese ores from Sandur, Karnataka, India. *Journal of*
603 *Mineralogy, Petrology, Economic Geology*, **91**, 46-61.
604 Monteiro, H.S., Vasconcelos, P.M.P., Farley, K.A. & Lopes, C.A.M. 2018. Age and evolution
605 of diachronous erosion surfaces in the Amazon: Combining (U-Th)/He and
606 cosmogenic ^{3}He records. *Geochimica et Cosmochimica Acta*, **229**, 162-183.
607 Nahon, D. 1986. Evolution of iron crusts in tropical landscapes. In Rates of chemical
608 weathering of rocks and minerals, S.M. Coleman and D.P. Dethier, Eds., Academic
609 Press, London, 169-191.
610 Najman, Y., Appel, E., Boudgher-Fadel M., Brown, P., Carter, A., Garzanti, E., Godin, L.,

Han, J., Liebke, U., Oliver, G., Parrish, R. & Vezzoli, G. Timing of India-Asia collision: Geological, biostratigraphic, and palaeomagnetic constraints. *Journal of Geophysical Researc*h, **115**, B12416.

Parc, S., Nahon, D., Tardy, Y. & Vieillard, P. 1989. Estimated solubility products and fields of stability for cryptomelane, nsutite, birnessite, and lithiophorite based on natural lateritic weathering sequences. *American Mineralogist*, **74**, 466-475.

Partridge, T.C. & Maud, R.R. 1987. Geomorphic evolution of southern Africa since the Meozoic. *South African Journal of Geology*, **90**, 179-208.

Prasad, G. 1983. A review of the early Tertiary bauxite event in South America, Africa and India. *Journal of African Earth Sciences*, **1**, 305–313.

Radhakrishna, B.P., 1993. Neogene uplift and geomorphic rejuvenation of the Indian Peninsula. *Current Science*, **64**, 787–793.

Ramstein, G., Khodri, M., Donnadieu, Y., Fluteau, F. & Goddéris, Y. 2005. Impact of the hydrological cycle on past climate changes: three illustrations at different time scales. *Comptes Rendus Geoscience*, **337**, 125–137.

Renne, P.R., Balco, G., Ludwig, K.R., Mundil, R. & Min, K. 2011. Response to the comment by W.H. Schwarz *et al.* on 'Joint determination of ^{40}K decay constants and ^{40}Ar*/^{40}K for the Fish Canyon sanidine standard, and improved accuracy for ^{40}Ar/^{39}Ar geochronology' by P.R. Renne *et al.* (2010). *Geochimica et Cosmochimica Acta*, **75**, 5097–5100.

Retallack, G.J. 2010. Lateritization and Bauxitization Events. *Economic Geology*, **105**, 655–667.

Richards, F.D., Hoggard, M.J. & White, N.J., 2016. Cenozoic epeirogeny of the Indian peninsula. *Geochemistry, Geophysics, Geosystems*, **17**, 4920–4954.

Riffel, S.B., Vasconcelos, P.M., Carmo, I.O. & Farley, K.A. 2015. Combined ^{40}Ar/^{39}Ar and

(U–Th)/He geochronological constraints on long-term landscape evolution of the Second Paraná Plateau and its ruiniform surface features, Paraná, Brazil. *Geomorphology*, **233**, 52–63.

Rivera, T.A., Storey, M., Zeeden, C., Hilgen, F.J. & Kuiper, K. 2011. A refined astronomically calibrated $^{40}Ar/^{39}Ar$ age for Fish Canyon sanidine. *Earth and Planetary Science Letters*, **311**, 420–426.

Roddick, J.C., Cliff, R.A. & Rex, D.C. 1980. The evolution of excess argon in alpine biotites-A ^{40}Ar-^{39}Ar analysis. *Earth and Planetary Science Letters*, **48**, 185–208.

Roy, S. 1981. Manganese Deposits, *Academic Press*. London, 458 p.

Ruffet, G., Innocent, C., Michard, A., Féraud, G., Beauvais, A., Nahon, D. & Hamelin, B. 1996. A geochronological $^{40}Ar/^{39}Ar$ and $^{87}Rb/^{81}Sr$ study of K-Mn oxides from the weathering sequence of Azul, Brazil. *Geochimica et Cosmochimica Acta*, **60**, 2219–2232.

Sawkar, R.H. 1981. Geology of the Manganese Ore Deposits of North Kanara District, Karnataka State, India, *Geology and Geochemistry of Managanese, II, Akademiai Kiadi,* Budapest, 281-295.

Sethumadhav, M.S., Gunnell, Y., Ahmed, M.M. & Chinnaiah. 2010. Late Archean manganese mineralization and younger supergene manganese ores in the Anmod-Bisgod region, Western Dharwar Craton, southern India: Geological characterization, palaeoenvironmental history, and geomorphological setting. *Ore Geology Reviews*, **38**, 70–89.

Shivaprakash, C. 1983. Petrology of quartzofeldspathic schists and phyllites associated with manganese formations of North Kanara and Kumsi, Karnataka. *Journal of the Geological Society of India*, **24**, 571–587.

Shuster, D.L., Vasconcelos, P.M., Heim, J.A. & Farley, K.A. Weathering geochronology by

659 (U-Th)/He dating of goethite. *Geochimica et Cosmochimica Acta*, **69** (3), 659-673.
660 Subramanian, K.S. & Mani, G. 1979. Geomorphic significance of lateritic bauxite in the
661 Shevaroy and Kollaimalai hills, Salem district, Tamil Nadu. *Journal Geological Society*
662 *of India*, **20**, 282-289.
663 Tardy, Y. 1997. Petrology of Laterites and Tropical Soils, *Balkema*. Rotterdam, 408 p.
664 Tardy, Y. & Roquin, C. 1992. Geochemistry and evolution of lateritic landscapes. In
665 Westhering, Soils & Paleosols, I.P. Martini & W. Chesworth, Eds., *Developments in*
666 *Earth Surface Processes* 2, **16**, 407-443.
667 Tardy, Y. & Roquin, C. 1998. *Dérive des continents. Paléoclimats et altérations tropicales,*
668 *Éd. BRGM*. Orléans, 473 p.
669 Thomas, M.F. 1994. Geomorphology in the Tropics: A Study of Weathering and Denudation
670 in Low Latitudes, *John Wiley & Sons Ltd*. Chichester, England, 482 p.
671 Valeton, I. 1999. Saprolite-bauxite facies of ferralitic duricrusts on palaeosurfaces of former
672 Pangea. *Special Publications of the international Association of Sedimentologists*, **27**,
673 153–188.
674 Vasconcelos, P.-M. 1999. K-Ar and $^{40}Ar/^{39}Ar$ geochronology of weathering processes.
675 *Annual Review of Earth and Planetary Sciences*, **27**, 183–229.
676 Vasconcelos, P.M. & Carmo, I. de O. 2018. Calibrating denudation chronology through
677 $^{40}Ar/^{39}Ar$ weathering geochronology. *Earth-Science Reviews*, **179**, 411–435.
678 Vasconcelos, P.M. & Conroy, M. 2003. Geochronology of weathering and landscape
679 evolution, Dugald River valley, NW Queensland, Australia. *Geochimica et*
680 *Cosmochimica Acta*, **67**, 2913–2930.
681 Vasconcelos, P.M., Heim, J.A., Farley, K.A., Monteiro, H. & Waltenberg, K. 2013. $^{40}Ar/^{39}Ar$
682 and (U–Th)/He – $^{4}He/^{3}He$ geochronology of landscape evolution and channel iron

683 deposit genesis at Lynn Peak, Western Australia. *Geochimica et Cosmochimica Acta*,
684 **117**, 283–312.
685 Vasconcelos, P.M., Renne, P.R., Becker, T.A. & Wenk, H.-R. 1995. Mechanisms and kinetics
686 of atmospheric, radiogenic, and nucleogenic argon release from cryptomelane during
687 $^{40}Ar/^{39}Ar$ analysis. *Geochimica et Cosmochimica Acta*, **59**, 2057–2070.
688 Widdowson, M. 1997. Tertiary paleosurfaces of the SW Deccan, Western India: implication
689 for passive margin uplift. M. Widdowson (Ed.), Palaeosurfaces: Recognition,
690 Reconstruction and Palaeoenvironmental Interpretation. *Geological Society Special*
691 *Publication*, London, 221–248.
692 Widdowson, M. & Gunnell, Y., 1999. Tertiary palaeosurfaces and lateritization of the coastal
693 lowlands of Western Peninsula India. in Palaeoweathering, Palaeosurfaces and Related
694 Continental Deposits, Edited by Médard Thiry and Régine Simon-Coinçon, Special
695 Publication, **27**, 245–274.
696 Zachos, J.C., Dickens, G.R. & Zeebe, R.E. 2008. An early Cenozoic perspective on
697 greenhouse warming and carbon-cycle dynamics. *Nature*, **451**, 279–283.
698
699 **FIGURES AND TABLE CAPTION**
700
701 **Fig. 1**. (**a**) Simplified geology (adapted from Bonnet et al., 2016 based on Chardon et al.,
702 2008) of the western part of Peninsular India, and (**b**) 30 m SRTM topography. Location of
703 studied area (North Kanara region) is shown.
704
705 **Fig. 2**. (**a**) Geological map of the study area in North Kanara region with the three
706 morphogeological strips upon which Mn ore deposits formed; (**b**) Topo-geomorphologic map
707 of the region showing the distribution area of remnants of three major landsurfaces, S1, S2,

708 and S3, with location of the studied/dated Mn ore deposits; **(c)** Synthetic geomorphogical
709 section across the study area in upstream Kali river drainage basin (section lines shown in Fig.
710 2b). Vertical exaggeration = 4.
711
712 **Fig. 3**. 3-D distribution of relicts of the three major lateritic landsurfaces of the Western Ghats
713 landscape, S1, S2, and S3; (**a**) Google-Earth view showing the landscape geomorphology
714 around the Terali Mn ore deposit, TER, (Image Landsat/Copernicus, Image©2018
715 DigitalGlobe); (**b**) Geomorphological interpretation map of this image. The altitudes are those
716 given by Google Earth (black dots).
717
718 **Fig. 4**. Field characteristics and petrographic structures of sample DIG-1 collected in the
719 Diggi Mn ore deposits. (**a**) Diggi open cast mine; (**b**) sample DIG-1 showing infiltration Mn
720 ore in iron duricrust; (**c**) Polished thin section of sample DIG-1A; (**d**) microscopic observation
721 of the polished thin section showing the colloform structure of infiltration Mn ore (C=
722 cryptomelane; Li= lithiophorite; ns= nsutite G= goethite); (**e**) micro X-ray fluorescence
723 analysis showing cryptomelane (C) and goethite (G) determined from a colour code, blue
724 (Mn) and green (K), and iron in red; (**f**) Scanning Electron Microscopy (SEM) image of
725 cryptomelane "needles"; (**g**) X-ray diffraction diagram of the sample powder.
726
727 **Fig. 5**. Micro-chemical compositions of cryptomelane obtained by electron probe
728 microanalyses (EPMA) distributed in a ternary diagram whose poles are Mn, 10 K and 10 Al.
729
730 **Fig. 6**. $^{40}Ar/^{39}Ar$ age spectra of crytpomelane grains from Mn ore deposits of (**a**) Diggi and
731 (**b**) Illva, with K/Ca (black) and Ar* (grey) step curves. (SS = Saddle shape)

732

733 **Fig. 7**. $^{40}Ar/^{39}Ar$ age spectra of crytpomelane grains from Mn ore deposits of (**a**) Terali, and
734 (**b**) Pradhani, with K/Ca (black) and Ar* (grey) step curves. (HS = Hump shape; SD = Stair
735 case degassing; SS = Sadde shape)

736

737 **Fig. 8**. $^{40}Ar/^{39}Ar$ age spectra of crytpomelane grains from Mn ore deposits of (**a**) Nagari, and
738 (**b**) Pradhani, with K/Ca (black) and Ar* (grey) step curves. (HS = Hump shape)

739

740 **Fig. 9**. Synthesis of the $^{40}Ar/^{39}Ar$ ages results with individual ages probability curves
741 accounting for results from this study and previous ones (Bonnet *et al.*, 2016). Each age
742 probability curve accounts for 1/3 of the total signal integrating individual ages degassing at
743 least 5% ^{39}Ar from all the preferred calculated ages (table. 1) weighted by the error margin for
744 the three sites (N_{Sandur} = 19 ages, $N_{Shimoga}$ = 10 ages; $N_{This\ study}$ = 38 ages). The calculated ages
745 are also plotted against the altitude. Altogether, the probability curves and the calculated ages
746 document major weathering peaks and periods W1, W2 and W3 (vertical colour bands),
747 which are compared to major trends of the global paleoclimatic curve (from Zachos *et al.*,
748 2008). PETM = Paleocene-Eocene Thermal Maximum; EECO = Early Eocene Climatic
749 Optimum; MECO = Mid-Eocene Climatic Optimum; EOC = Early Oligocene Cooling;
750 LOW= Late Oligocene Warming; MMCO = Mid-Miocene Climatic Optimum. Ages in bold
751 and arrowed are terminal ages of weathering periods W1 to W3.

752

753 **Fig. 10**. Landscape and lateritic weathering dynamical evolution in Western Ghats of
754 Peninsular India illustrating early cryptomelane-rich Mn ores formation at **(a)** the first
755 bauxitic step S1 (red), and their preservation over the Cenozoic at each next landscape **(b)**

stage S2 (in blue), and **(c)** S3 pediment (in green). Coloured dashed lines represent successive weathering fronts of S1, S2 and S3 profiles. After 10 Ma, the S3 landscape is dissected.

Table 1. Synthesis of the $^{40}Ar/^{39}Ar$ ages calculated from plateaus in ^{39}Ar release spectra and isochrons, with the integrated and the preferred ages.

A		^{39}Ar release spectrum			Isochrone					Integrated Age	Preferred age	Comments
Sample ID	**Altitude (m)**	**Age ± 2σ, Ma**	**Step(s)**	**%^{39}Ar**	**Age ± 2σ, Ma**	**^{40}Ar/^{36}Ar**	**MSWD**	**Steps**	**%^{39}Ar**	**Age ± 2σ, Ma**	**Age ± 2σ, Ma**	
DIGGI												
DIG-1A-T4	623	12.3 ± 0.3	7-11	72	11.3 ± 0.5 11.1 ± 0.3	318 ± 10 298 ± 4	1.11 0.13	7-11 5-6, 12-14	72 21	12.0 ± 0.3	**12.3 ± 0.3**	Plateau > 70 % ^{39}Ar
DIG-1A-T5	623	11.6 ± 0.2	5-8	71	11.8 ± 0.2 11.6 ± 0.2	289 ± 5 298 ± 3	0.57 1.32	5-8 1-4, 7-8	71 62	11.7 ± 0.5	**11.6 ± 0.2**	Plateau > 70 % ^{39}Ar
DIG-1A-T6	623	12.3 ± 0.3	7-12	83	12.6 ± 0.2	284 ± 6	1.36	6-7, 9-10, 14-15, 17-18	58	12.4 ± 0.2	**12.3 ± 0.3**	Plateau > 70 % ^{39}Ar
DIG-1B-T2	623	13.3 ± 0.2	4-8	85	13.0 ± 0.7	302 ± 31	1.43	4, 6-8	61	13.3 ± 0.3	**13.3 ± 0.2**	Plateau > 70 % ^{39}Ar
DIG-1B-T3	623	13.3 ± 0.3	3-9	79	13.3 ± 0.4	296 ± 6	0.69	3-9	79	13.4 ± 0.5	**13.3 ± 0.3**	Plateau > 70 % ^{39}Ar
DIG-1B-T4	623	12.4 ± 0.2	9-13	74	12.4 ± 0.2	298 ± 3	1.19	2-3, 10-13	73	12.2 ± 0.5	**12.4 ± 0.2**	Plateau > 70 % ^{39}Ar
TERALI												
TER-1A-T1	644	28.7 ± 0.5	6-8	61	28.5 ± 0.4	289 ± 7	2.41	1-4, 6, 8-9	63	28.2 ± 0.5	**28.7 ± 0.5**	Min of oldest Forced plateau > 50 % 39Ar
TER-1A-T2	644	32.3 ± 0.4	11-14	49	22.6 ± 0.6	289 ± 3	0.61	2-5, 7-8	10	31.5 ± 0.9	**32.3 ± 0.4**	Min of oldest Forced plateau < 50 % 39Ar
TER-1B-T3	644	27.5 ± 0.3	6-8	73	27.8 ± 0.2	278 ± 4	2.88	1, 3, 6-7, 12	63	26.7 ± 1.2	**27.5 ± 0.3**	Min of oldest Plateau > 70 % 39Ar

B		^{39}Ar release spectrum			Isochrone					Integrated Age	Preferred age	Comments
Sample ID	**Altitude (m)**	**Age ± 2σ, Ma**	**Step(s)**	**%^{39}Ar**	**Age ± 2σ, Ma**	**^{40}Ar/^{36}Ar**	**MSWD**	**Steps**	**%^{39}Ar**	**Age ± 2σ, Ma**	**Age ± 2σ, Ma**	
NAGARI												
NAG-1B-T2	520	32.0 ± 1.9 41.2 ± 1.4	1-4 5-7	50 50	32.4 ± 2.0	293 ± 6	0.78	1-4, 7	52	38.0 ± 3.4	**32.4 ± 2.0**	Best fitted isochrone
NAG-3A-T3	520	31.3 ± 0.1	9-11	24	31.6 ± 1.1 50.3 ± 0.4	295 ± 2 292 ± 1	2.07 1.1	3-4, 9-12 1-2, 5, 7	32 42	43.8 ± 4.5	**31.6 ± 1.1**	Best fitted isochrone
NAG-3B-T1	520	45.0 ± 1.0	7-11	53	40.6 ± 1.6	301 ± 4	0.5	2-6, 10-11	49	44.3 ± 1.3	**45.0 ± 1.0**	Plateau > 50 % ^{39}Ar
NAG-3B-T2	520	44.0 ± 0.9	4-6	78	44.3 ± 0.8	299 ± 4	1,74	2, 4-5	58	43.6 ± 1.3	**44.0 ± 0.9**	Min of oldest Plateau > 70 % ^{39}Ar
NAG-3B-T3	520	44.9 ± 3.6	8-10	52	35.3 ± 4.7 46.4 ± 2.6	297 ± 16 297 ± 5	0.25 1.88	7, 11-14 5-6, 8-9	28 43	43.2 ± 2.9	**44.9 ± 3.6**	Forced plateau > 50 % ^{39}Ar

TABLE. 1a-b

C		^{39}Ar release spectrum			Isochrone					Integrated Age	Preferred age	Comments
Sample ID	Altitude (m)	Age ± 2σ, Ma	Step(s)	%^{39}Ar	Age ± 2σ, Ma	^{40}Ar/^{36}Ar	MSWD	Steps	%^{39}Ar	Age ± 2σ, Ma	Age ± 2σ, Ma	
ILLVA												
ILV-1B-T4	524	12.7 ± 0.8	2-8	92	12.7 ± 0.9	296 ± 9	1.11	2-8	92	12.6 ± 0.8	**12.7 ± 0.8**	Plateau > 70 % ^{39}Ar
ILV-1B-T5	524	12.3 ± 0.1	6-9	73	12.3 ± 0.1	298 ± 3	1.22	2, 7-9	57	12.3 ± 0.5	**12.3 ± 0.1**	Plateau > 70 % ^{39}Ar
ILV-2C-T3	524	12.1 ± 1.3	1-9	100	12.1 ± 1.6	29 ± 40	0.14	1, 4-6, 8	82	12.1 ± 1.3	**12.1 ± 1.3**	Plateau > 70 % ^{39}Ar
ILV-2C-T4	524	12.9 ± 0.3	7-9	70	12.9 ± 0.7	295 ± 48	0.46	6-9	85	12.9 ± 0.3	**12.9 ± 0.3**	Plateau > 70 % ^{39}Ar
ILV-3A-T1	524	13.1 ± 0.4	6-7	63	13.2 ± 0.2	300 ± 7	2.7	5- 6, 10-12	48	13.1 ± 0.2	**13.1 ± 0.4**	Forced plateau > 50%
ILV-3A-T3	524	14.0 ± 0.7	6-10	76	14.0 ± 0.8	304 ± 79	0.4	7-9	66	14.1 ± 2.9	**14.0 ± 0.7**	Plateau > 70 % ^{39}Ar
ILV-3C-T4	524	13.6 ± 0.3	1-6	65	13.5 ± 0.3	294 ± 16	1.14	3-6, 8	61	13.7 ± 0.4	**13.6 ± 0.3**	Plateau > 50 % ^{39}Ar
ILV-6A-T1	524	11.3 ± 0.1	9-11	50	11.3 ± 0.1	293 ± 2	1.84	1-3, 4-5, 9-11	59	11.6 ± 0.7	**11.3 ± 0.1**	Best fitted isochrone
ILV-6A-T2	524	11.6 ± 0.2	8-11	79	11.4 ± 0.1	296 ± 3	0.94	3, 7, 10-11, 14-15	42	11.6 ± 0.2	**11.6 ± 0.2**	Plateau > 70 % ^{39}Ar
ILV-6A-T3	524	10.0 ± 0.2	7-9	84	10.1 ± 0.1	297 ± 6	0.45	1, 4, 6, 8-9	56	10.0 ± 0.2	**10.0 ± 0.2**	Plateau > 70 % ^{39}Ar
ILV-6B-T1	524	11.0 ± 0.1	7-9	55	11.0 ± 0.1	289 ± 4	2.85	2-3, 7-9, 12	64	11.1 ± 0.2	**11.0 ± 0.1**	Pseudo-Plateau > 50 % ^{39}Ar
ILV-6B-T2	524	14.4 ± 0.4	7-9	62	14.5 ± 0.1	292 ± 2	1.24	3-5, 7, 9	55	14.0 ± 1.0	**14.5 ± 0.1**	Best fitted isochrone
ILV-6B-T3	524	12.0 ± 0.2	8-11	66	11.9 ± 0.2	310 ± 6	0.99	5, 8-11	69	12.8 ± 0.8	**12.0 ± 0.2**	Plateau > 50 % ^{39}Ar
PRADHANI												
PRA-1B-T1	620	25.2 ± 0.2	5-6	61	-	-	-	-	-	25.2 ± 1.7	**25.2 ± 0.2**	Pseudo-Plateau > 50 % ^{39}Ar
PRA-1B-T2	620	29.8 ± 0.4	8-10	48	24.2 ± 0.2	276 ± 3	1.21	2, 4-5	8	28.6 ± 4.2	**29.8 ± 0.4**	Forced plateau < 50 % ^{39}Ar
PRA-1B-T3	620	45.4 ± 0.9	7-9	50	30.8 ± 1.7 44.9 ± 0.6	277 ± 8 289.5 ± 27	0.96 2.13	2-4, 12 1, 7, 9, 11	18 40	43.8 ± 2.2	**45.4 ± 0.9**	Forced plateau ~ 50 % ^{39}Ar
PRA-2A-T1	620	24.5 ± 0.2	7-9	58	24.6 ± 0.2	252 ± 19	4.7	2, 7-9	60	24.5 ± 0.6	**24.5 ± 0.2**	Plateau > 50 % ^{39}Ar
PRA-2A-T3	620	23.7 ± 0.2	10-16	78	23.7 ± 0.2	272 ± 28	0.44	1, 3, 10-14	61	23.7 ± 0.4	**23.7 ± 0.2**	Plateau > 70 % ^{39}Ar
PRA-2A-T5	620	21.6 ± 0.1	9-15	79	21.6 ± 0.1	294 ± 9	1.07	1-2, 9-16	81	21.5 ± 0.3	**21.6 ± 0.1**	Plateau > 70 % ^{39}Ar
PRA-2B-T1	620	27.8 ± 0.2	15-22	59	20.3 ± 1.1	294 ± 11	0.84	4, 7-11	11	27.5 ± 0.6	**27.8 ± 0.2**	Plateau > 50 % ^{39}Ar
PRA-2B-T2	620	22.4 ± 0.2	12-15	47	19.9 ± 0.6	292 ± 20	1.05	2, 5-7	4	22.5 ± 0.4	**22.4 ± 0.2**	Forced plateau < 50 % ^{39}Ar
PRA-2B-T4	620	23.4 ± 0.1	9-12	62	21.2 ± 0.5	291 ± 1	4.81	3-6	6	23.6 ± 0.7	**23.4 ± 0.1**	Plateau > 50 % ^{39}Ar
PRA-3B-T1	620	32.8 ± 0.2	10-12	54	29.1 ± 0.7	277 ± 6	2.73	2-6	8	36.2 ± 4.3	**32.8 ± 0.2**	Plateau > 50 % ^{39}Ar
PRA-3B-T2	620	37.5 ± 0.5	11-13	58	28.7 ± 0.8	277 ± 4	1.1	1-3, 6-7	6	41.6 ± 8.7	**37.5 ± 0.5**	Forced plateau > 50 % ^{39}Ar

TABLE. 1c

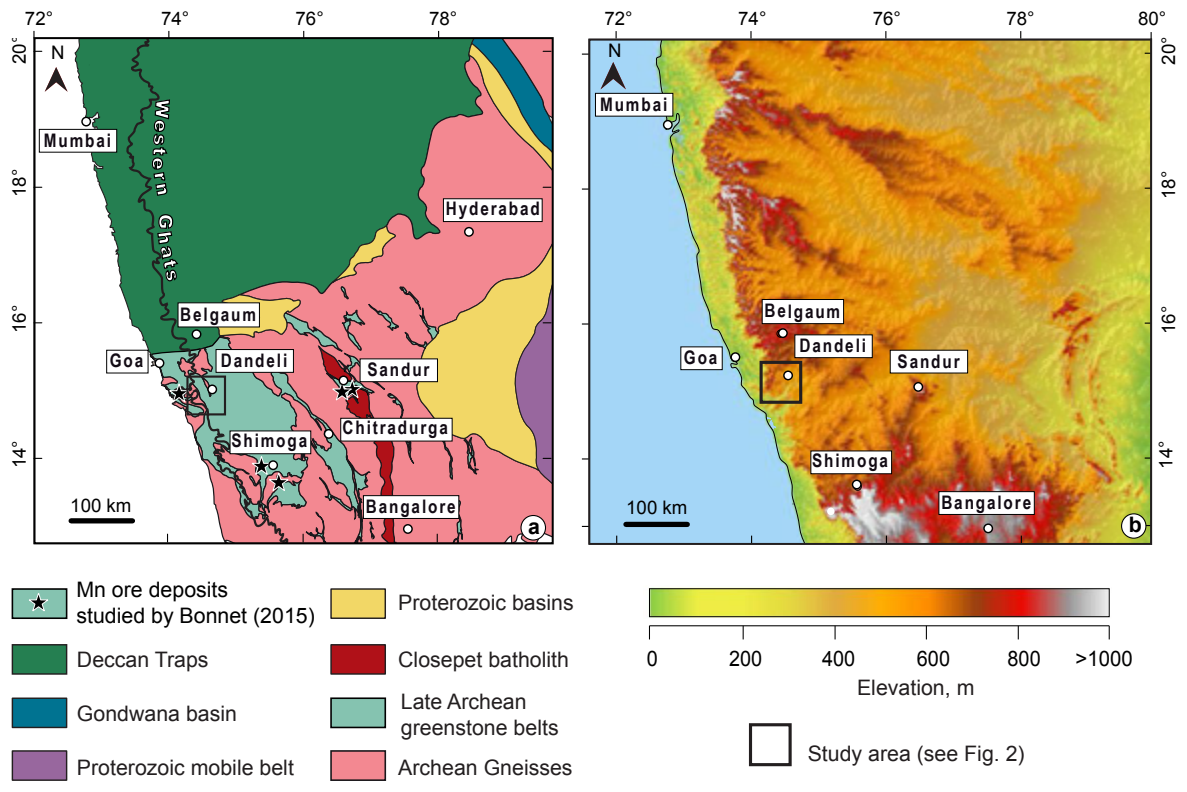

FIGURE. 1 (Jean et al., 2019)

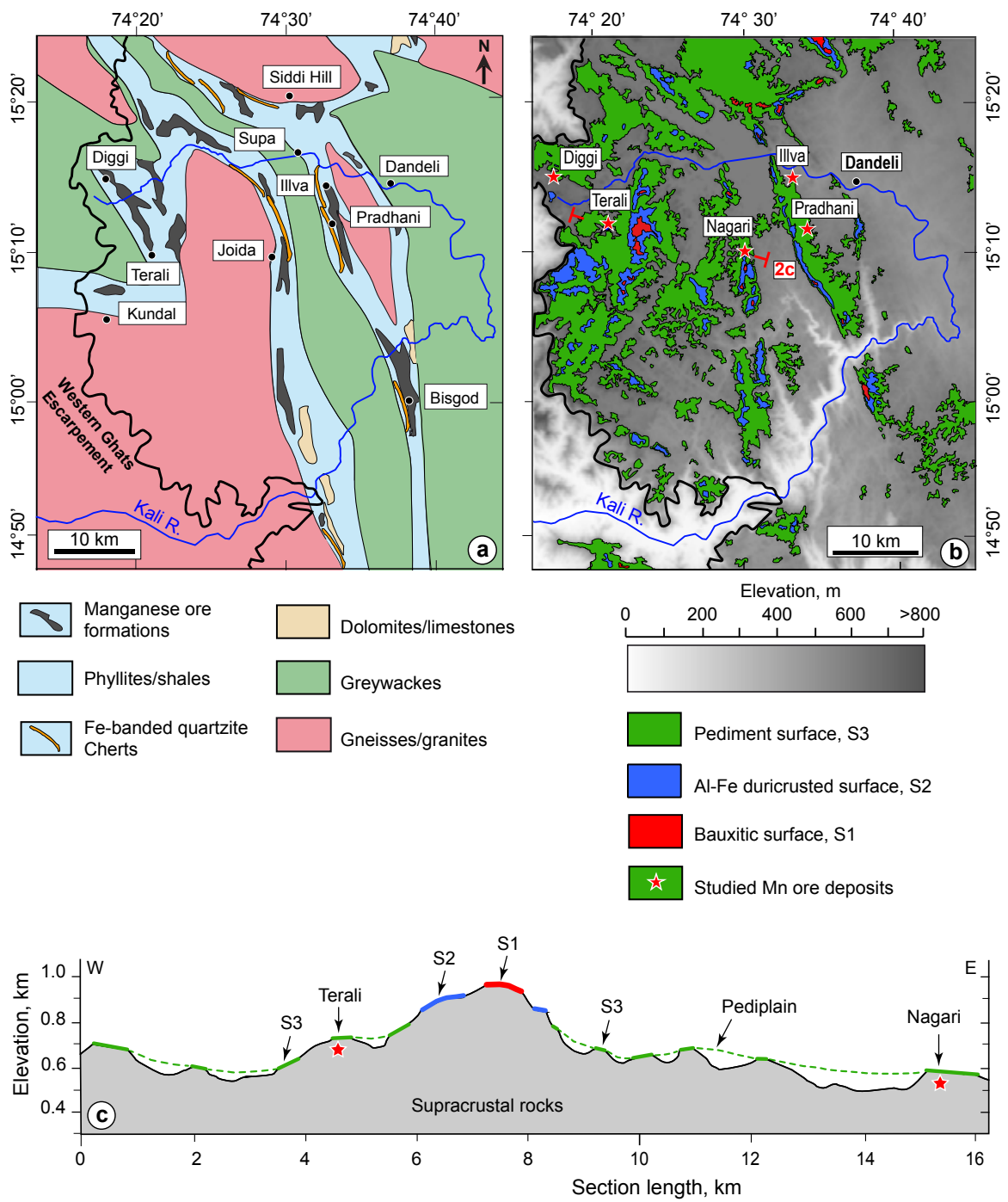

Figure. 2 (Jean et al., 2019)

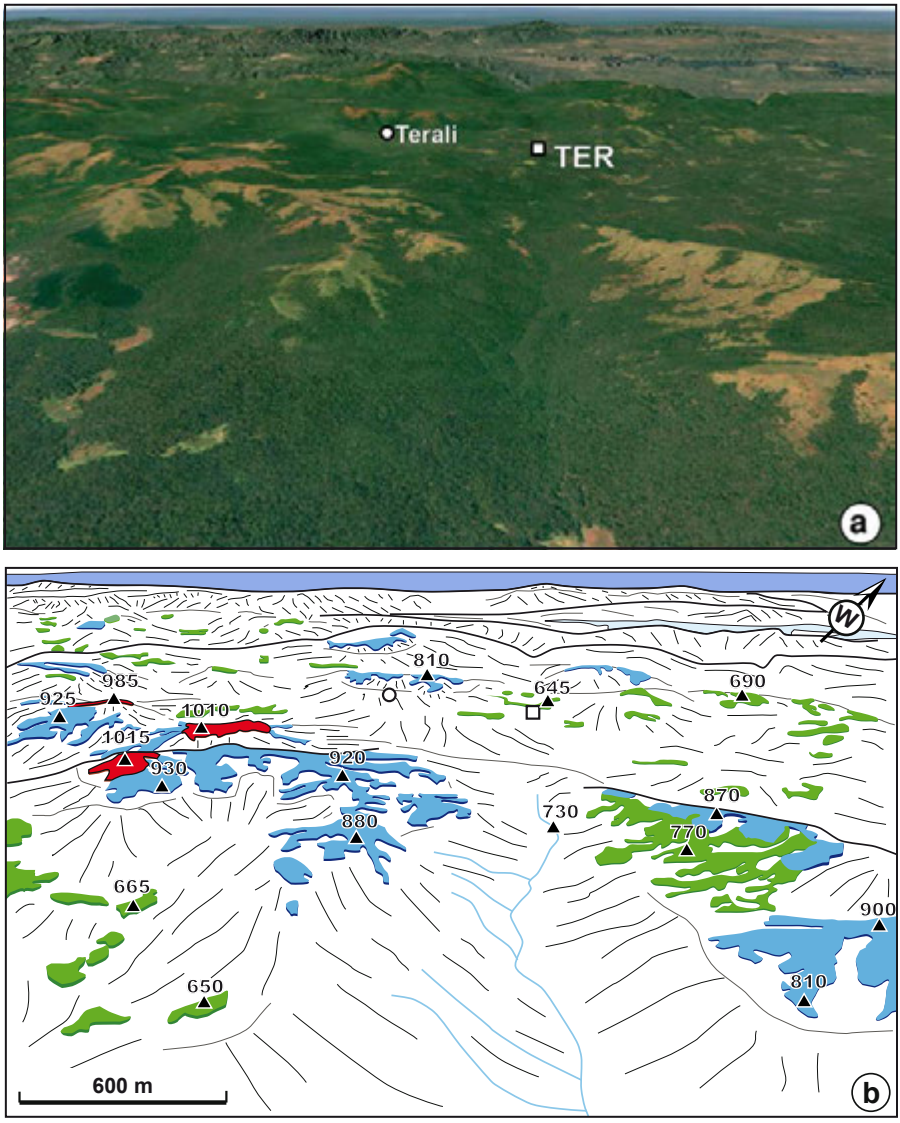

FIGURE. 3 (Jean et al., 2019)

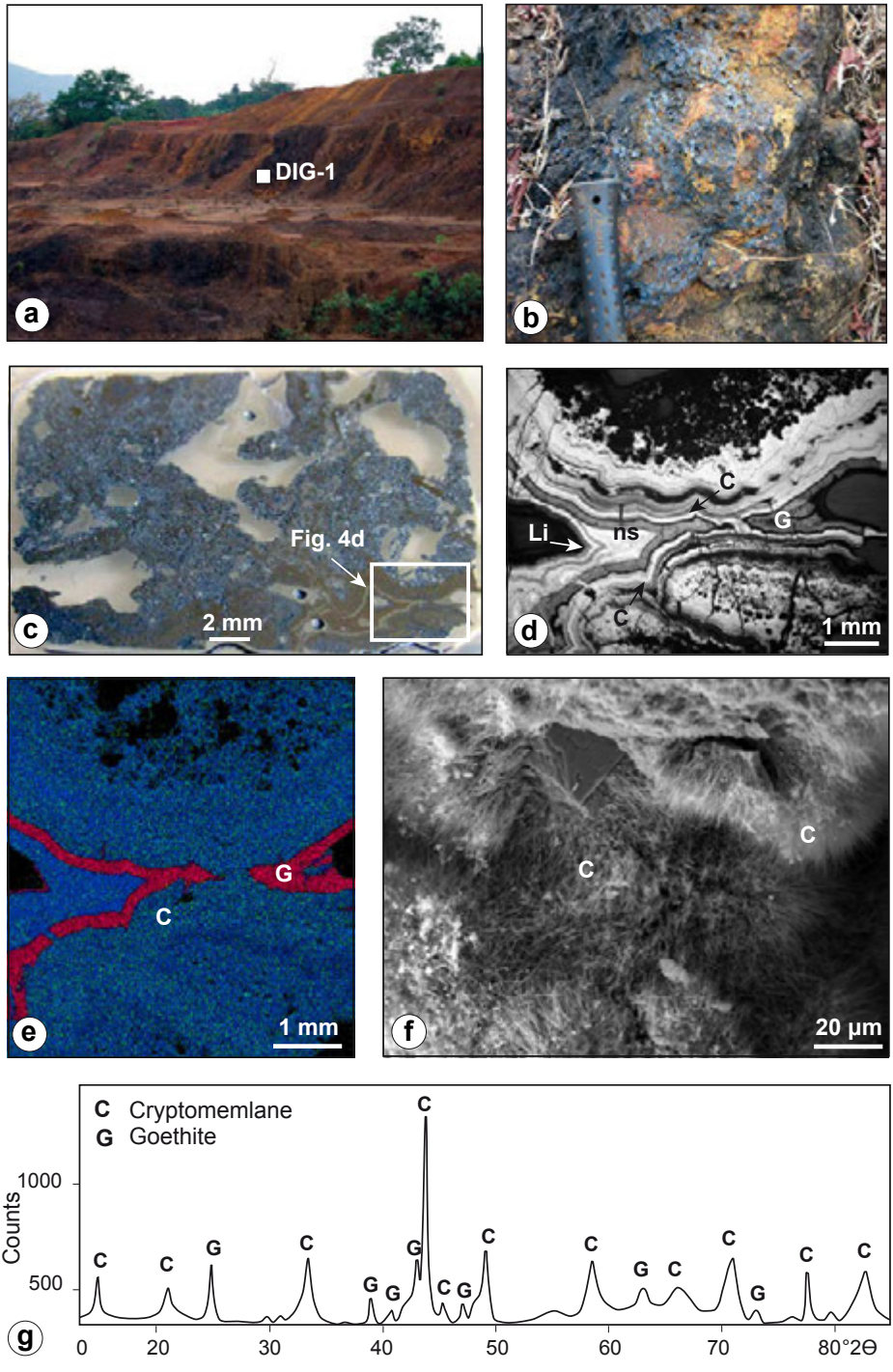

FIGURE. 4 (Jean et al., 2019)

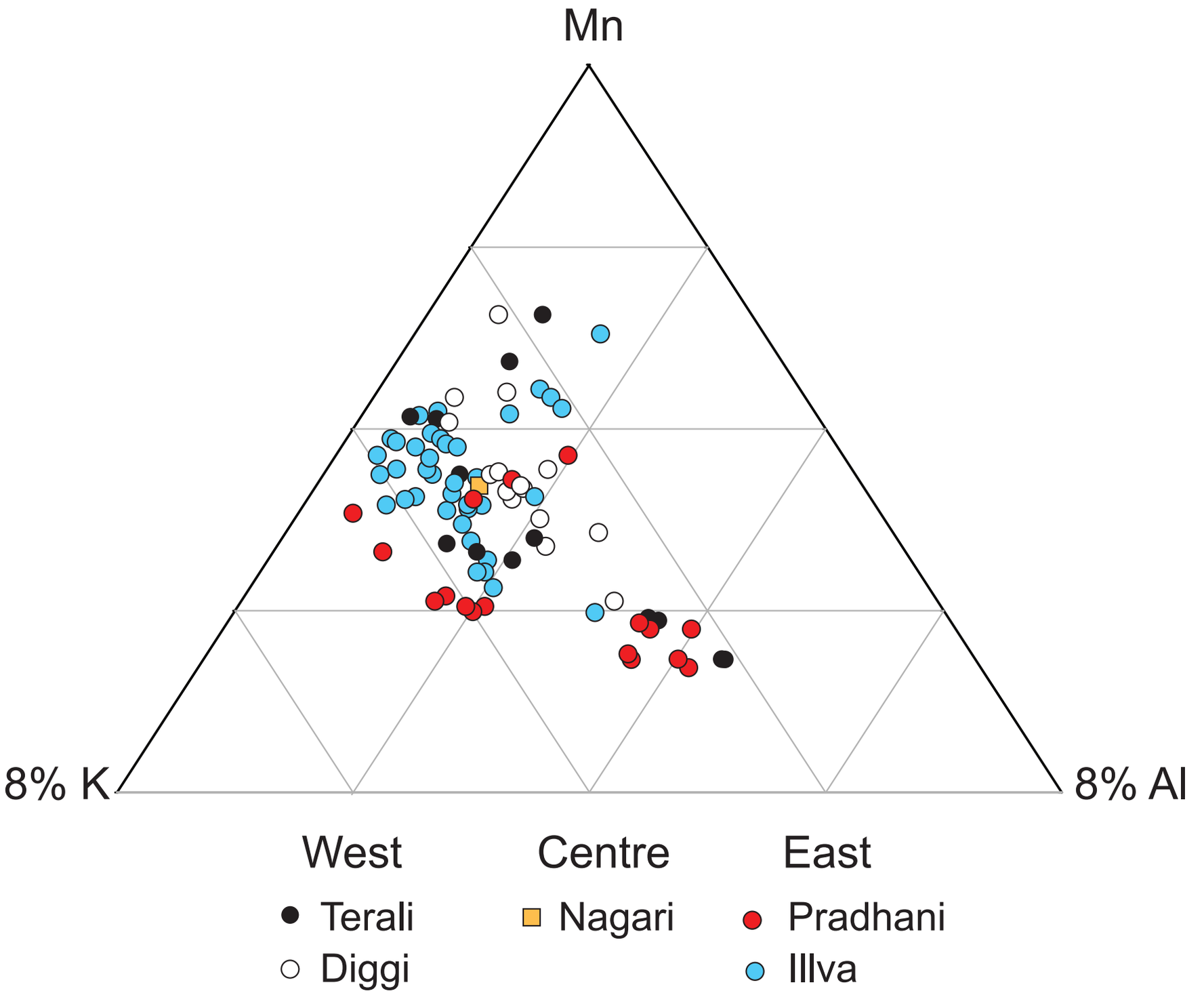

FIGURE. 5 (Jean et al., 2019)

FIGURE. 6 (Jean et al., 2019)

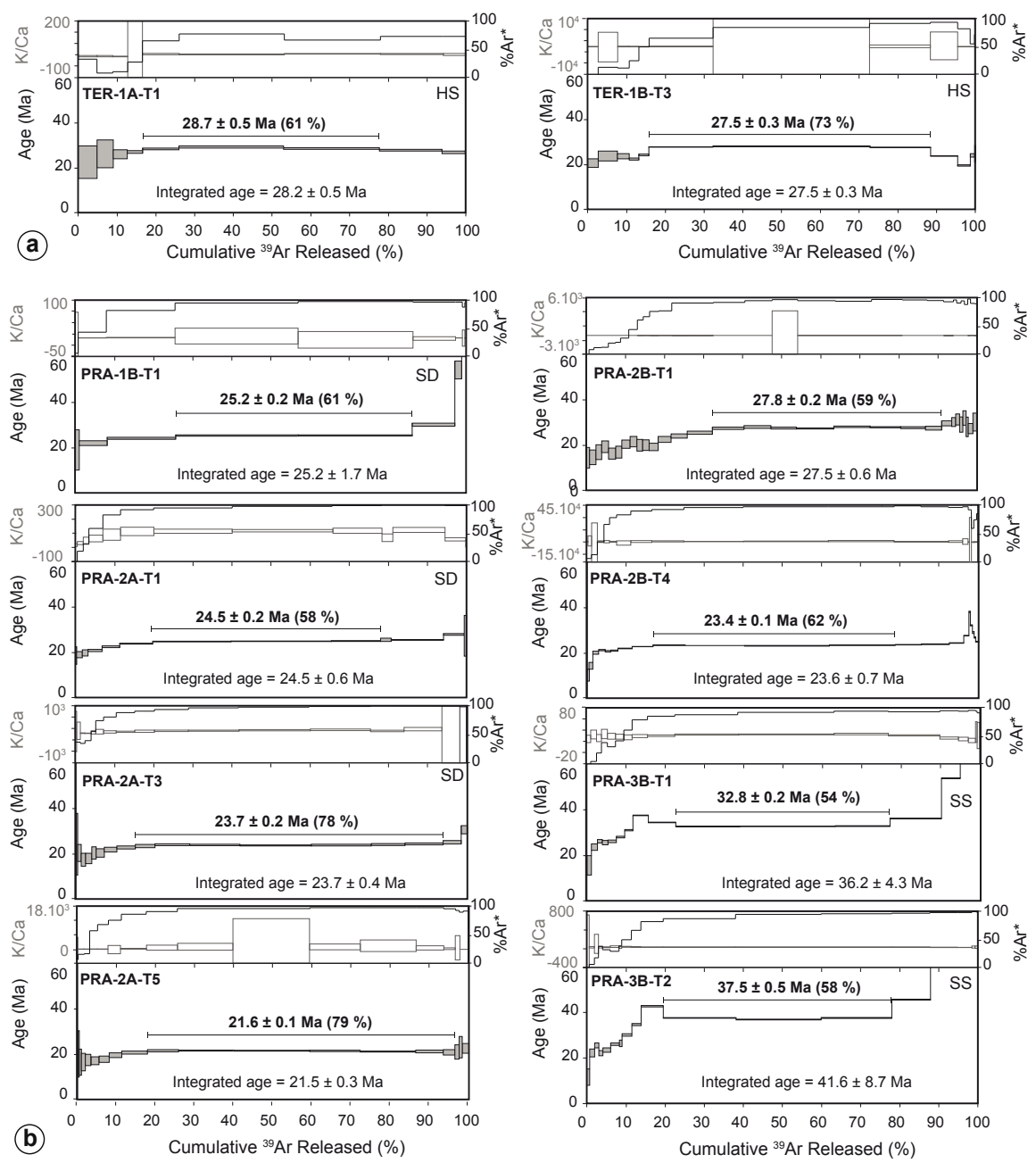

FIGURE. 7 (Jean et al., 2019)

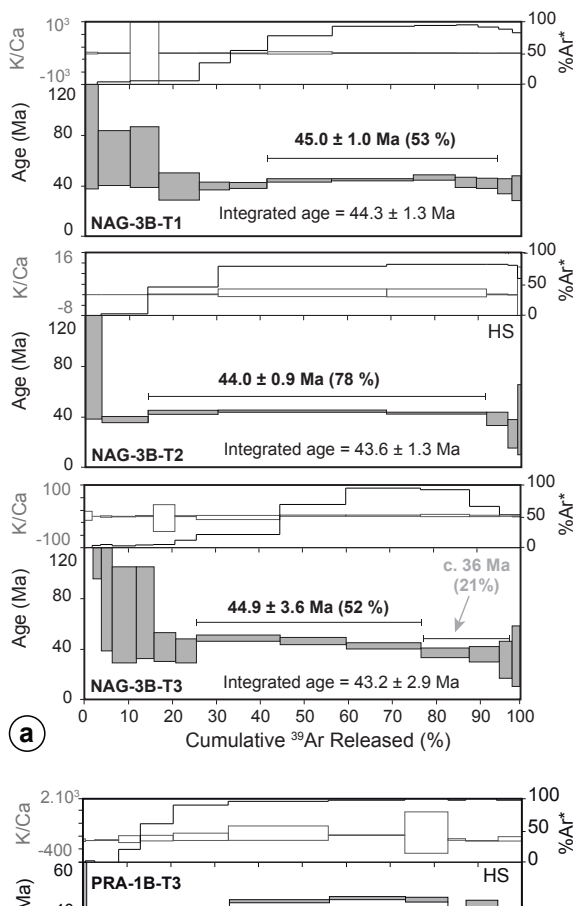

FIGURE. 8 (Jean et al., 2019)

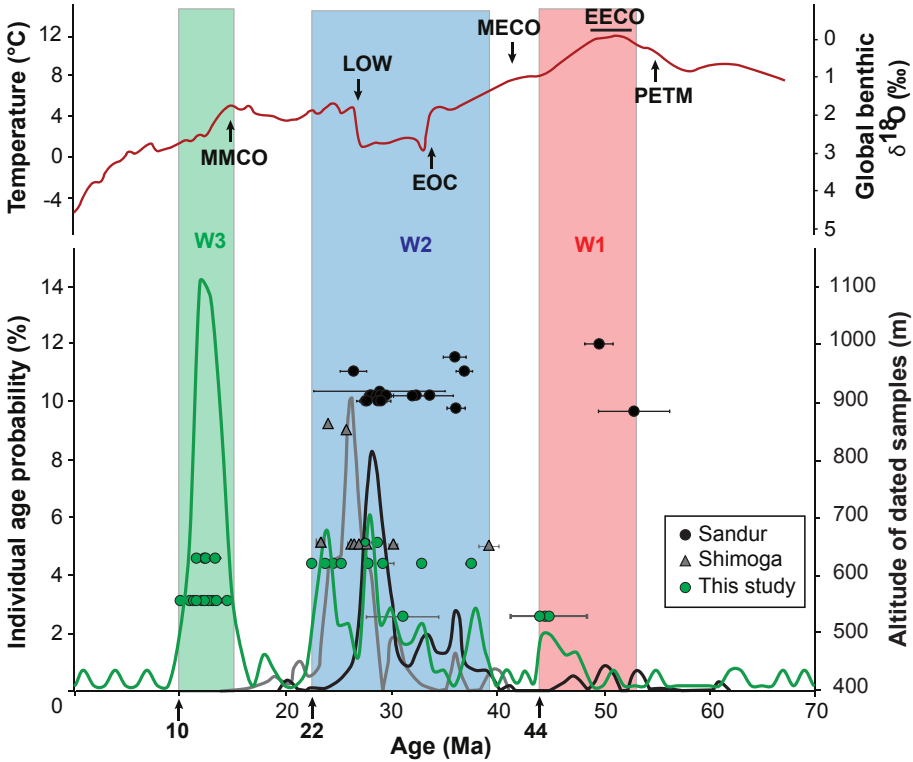

FIGURE. 9 (Jean et al., 2019)

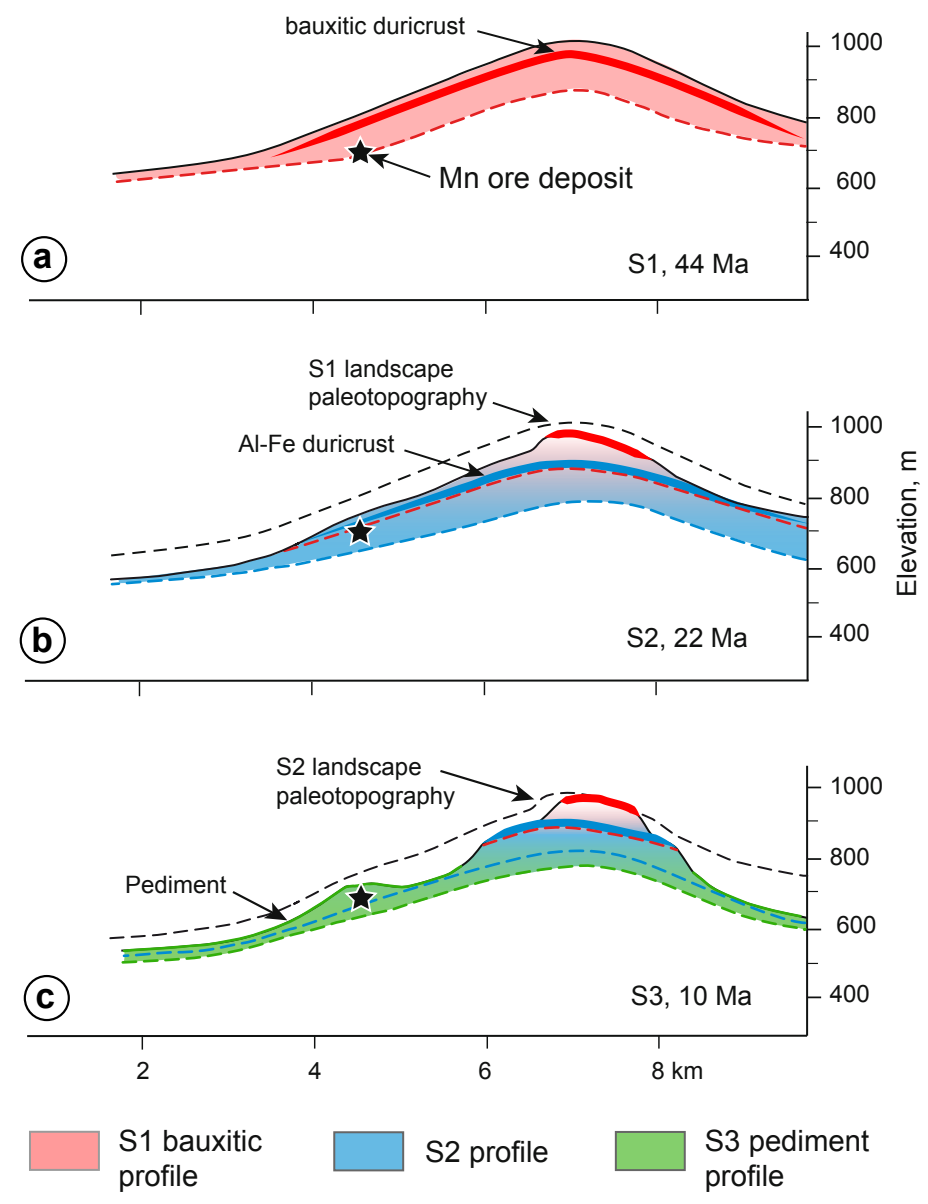

FIG. 10 (Jean et al., 2019)